Molecular Dynamics Analysis of 6H-SiC Subsurface Damage by Nanofriction

Dongling Yu,[§] Huiling Zhang,[§] Xiaoyu Feng, Dahai Liao, and Nanxing Wu*

Read Online

ACCESS | Metrics & More | Article Recommendations

ABSTRACT: To investigate the subsurface damage of 6H-SiC nanofriction, this paper uses molecular dynamics analysis to analyze the loading process of friction 6H-SiC surfaces, thus providing an in-depth analysis of the formation mechanism of subsurface damage from microscopic crystal structure deformation characteristics. This paper constructs a diamond friction 6H-SiC nanomodel, combining the radial distribution function, dislocation extraction method, and diamond identification method with experimental analysis to verify the dislocation evolution process, stress distribution, and crack extension to investigate the subsurface damage mechanism. During the friction process, the kinetic and potential energies as well as the temperature of the 6H-SiC workpiece basically tend to rise, accompanied by the generation of dislocated lumps and cracks on the sides of the 6H-SiC workpiece. The stresses generated by friction during the plastic deformation phase lead to dislocations in the vicinity of the diamond tip friction, and the process of dislocation nucleation expansion is accompanied by energy exchange. Dislocation formation is found to be the basis for crack generation, and cracks and peeled blocks constitute the subsurface damage of 6H-SiC workpieces by diamond identification methods. Friction experiments validate microscopic crystal changes against macroscopic crack generation, which complements the analysis of the damage mechanism of the simulated 6H-sic nanofriction subsurface.
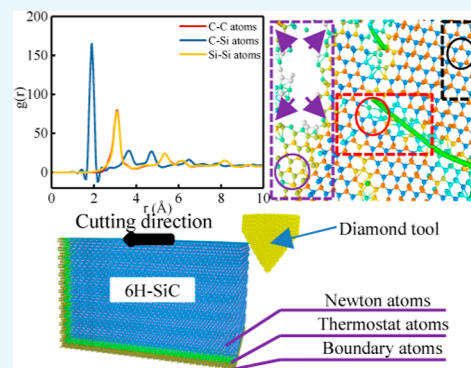
1. INTRODUCTION

6H-SiC is characterized by high hardness,[1] high stiffness,[2] and a high forbidden band width[3] and is widely used in high-temperature, high-radiation aerospace[4] and high-voltage, high-magnetic-field optoelectronic integration[5] as well as biomedical applications.[6] Conventional grinding methods can no longer meet the requirements of nanoscale machining[7] and efficient and high precision of atomic-level 6H-SiC materials with the development of the ultra-precision manufacturing technology. The ultra-precision machining technology[8,9] is one of the effective methods to achieve non-destructive machining. The ultra-hardness and brittleness of 6H-SiC[10,11] and the damage caused by defects such as crystal fracture, crystalline transformation, dislocation slip, and microcracking during reworking[12−15] affect the performance of machined parts. The temperature gradient of friction, friction parameters, and parameter changes of residual stresses can affect the surface deformation damage of 6H-SiC to different degrees. The material contact surface stress generated by friction is the main cause of dislocation formation, and the extensional change of dislocation is the key to crack formation. An in-depth study of material removal mechanisms such as surface generation, subsurface damage, and tool wear during nanomachining of silicon carbide can not only improve the quality of mechanics of 6H-SiC materials but also promote the development of the product technology of 6H-SiC materials.

Some scholars are now exploring the performance characteristics of silicon carbide by means of high-precision lathe machining and polishing and finite element analysis to further investigate the formation mechanism of friction on subsurface damage at the nanoscale. Duan et al.[16] observed the removal process of single-crystal SiC by scratching with conical diamond abrasive grains with different tip fillet radii and found that the elastic−plastic deformation critical point and deformation mode change as the diamond radius increases, the brittle-plastic critical-brittle removal transition point[17] keeps getting deeper, the microcracks become longer, and the material damage form escalates. Tian et al.[18] explored the removal of subsurface defects from 6H-SiC surfaces by friction experiments based on molecular dynamics simulation methods and found that the deformation of the material consisted mainly of plastic amorphous transformation and dislocation slip and also found that less amorphous deformation of the C phase compared to Si indicated better material removal. Their

study lays the foundation for the selection of processing control parameters for optimal surface quality. Xiao et al.[19] performed a visualization study of 6H-SiC using reproduction of the interaction potential of high-temperature elastoplasticity of silicon carbide and found that the corresponding potential of elastoplasticity of 6H-SiC HPPT and dislocation activity act together, with dislocations playing a dominant role in crack damage. Greiner et al.[20] combined molecular dynamics simulation methods with friction experiments to observe the high-purity copper under friction loading the evolution of the peritectic structure, observing the activity of dislocations, as well as dislocation movement trajectories and subgrain boundaries of the core and found and hypothesized that the clusters formed on the surface after friction introduce a new stage of damage, while causing recrystallization of the surface due to rotational friction. The above studies show that subsurface damage is mostly caused by the formation of dislocations, and the nucleation expansion of dislocations becomes a breakthrough for exploring 6H-SiC, and the strength of the tool and subsurface damage of the workpiece are the focus of production processing. Therefore, the process and internal stress of 6H-SiC friction are deeply analyzed from the nano perspective, and the subsurface damage mechanism is analyzed in combination with experiments to further improve the precision of the 6H-SiC material processing process.

To investigate the subsurface damage of 6H-SiC nanofriction, this paper analyzes the loading process of the 6H-SiC nanofriction surface based on the molecular dynamics analysis method. The subsurface damage mechanism is investigated by analyzing the dislocation evolution, stress distribution, and crack extension. In order to investigate the surface friction of 6H-SiC and to gain insight into the subsurface damage mechanism, the friction process is monitored in real time by visualization software. This method is a guideline for the in-depth understanding of the surface friction mechanism of 6H-SiC and the improvement of the non-destructive processing technology of 6H-SiC.

2. 6H-SIC SIMULATION MODELING

2.1. Simulation Model Construction. To ensure the accuracy of the simulated friction process, a three-dimensional molecular dynamics model containing a yellow diamond abrasive and a blue silicon carbide workpiece was established, as shown in Figure 1.

The simulation does not take into account the deformation of the indenter and sets the indenter as a rigid body. The dimensions of the simulated box are 30 nm × 12 nm × 17 nm,
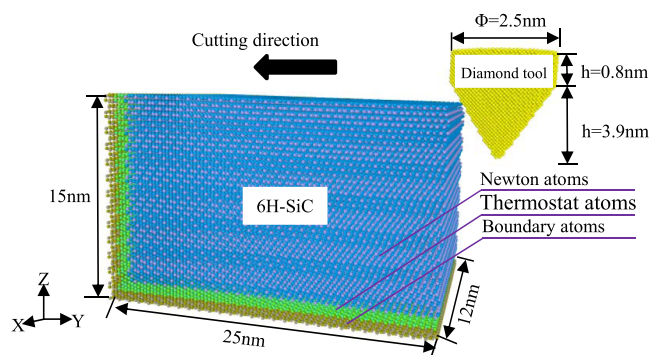
Figure 1. Simulation model of the 6H-SiC nano-orthogonal cutting.

the diameter of the indenter is 2.5 nm, the tip height is $h = 2.9$ nm, and the indenter extension length is 0.8 nm, containing a total of 9811 atoms. The 6H-SiC artifact has a size of 25 nm × 12 nm × 15 nm and contains a total of 389,207 atoms. To eliminate boundary disturbances in modeling, the X- and Z-directions are set as periodic boundary conditions and the Y-direction is set as the acyclic boundary condition.[21] To simulate the friction process more accurately, the 6H-SiC and diamond indenter atoms were divided into a thermostatic layer of atoms with a thickness of 1 nm and a boundary layer of atoms according to Newton's law of motion, where the boundary layer can fix the atomic boundaries and the thermostatic layer ensures the heat exchange of the internal atoms,[22] and the Newton layer in the figure is the atomic layer for the simulated friction test. Balint[23] et al. indicated that as a friction tool, the friction depth of diamond would have a certain impact on the deformation of the workpiece. When the friction depth of the tool is small relative to the thickness of the workpiece, the friction decreases and gradually increases with the increase of the contact depth and has little influence on the elastic field, and the effect of the shallow friction depth on the length of the dislocation is also small. Therefore, in order to ensure the accuracy of the simulation effect, reduce the influence of the tool on the friction effect, and facilitate the subsequent dislocation observation, the friction depth in this paper is set at 3 nm. The friction simulation test was performed along the negative direction of the Y-axis. The data are shown in Table 1.

Table 1. Simulation Parameters and Values of 6H-SiC Nanofriction

	parameter values
simulated box size	30 nm × 12 nm × 17 nm
tool diameter	2.5 nm
length of the tool tip	2.9 nm
number of atoms in the workpiece	9811
6H-SiC workpiece size	25 nm × 12 nm × 15 nm
number of atoms in the 6H-SiC workpiece	389,207
depth of the cutting	3 nm
cutting crystal	(0001)

2.2. Tersoff Potential Function. The selection of the potential function is an important issue in the field of studying molecular dynamics. The potential function determines the physical and chemical properties of the modeled material; therefore, the accuracy of the potential function selection determines the accuracy and precision of the simulation results. The Tersoff potential function[24] is based on quantum mechanics, where the interatomic bond levels depend on their own environment, and the stronger their bonds, the more accurately they can calculate the interatomic forces in covalent systems when there are more atoms around them. The Tersoff potential function is applicable to materials with more complex structures such as diamond and silicon carbide. 6H-SiC belongs to covalently bonded crystals, and the calculation of the interatomic potential energy should consider the interaction between the polyatomic covalent bonds. Therefore, the Tersoff potential function is used to describe the interaction forces of Si-Si, C-C, and C-Si atomic bonds in 6H-SiC, which is expressed as

$$V_{ij} = f_C(r_{ij} + \delta)[f_R(r_{ij} + \delta) + b_{ij}f_A(r_{ij} + \delta)] \tag{1}$$

The expression for the potential energy between atoms is

$$E = \frac{1}{2} \sum_i \sum_{j \neq i} ij \tag{2}$$

$$f_C(r) = \begin{cases} 1 & r < R - D \\ \frac{1}{2} - \frac{1}{2}\sin\left(\frac{\pi}{2}\frac{r-R}{D}\right) & R - D < r < R + D \\ 0 & R > R + D \end{cases} \tag{3}$$

$$f_R(r) = A \exp(-\lambda_1 r) \tag{4}$$

$$f_A(r) = B \exp(-\lambda_2 r) \tag{5}$$

$$b_{ij} = (1 + \beta^n \zeta_{ij}^n)^{-1/2} \tag{6}$$

$$\zeta_{ij} = \sum_{k \neq i,j} f_C(r_{ik} + \delta)g[\theta_{ijk}(r_{ij}, r_{ik})]\exp[\lambda_3^m(r_{ij} - r_{ik})^m] \tag{7}$$

$$g(\theta) = \gamma_{ijk}\left(1 + \frac{c^2}{d^2} - \frac{c^2}{[d^2 + (\cos\theta - \cos\theta_0)^2]}\right) \tag{8}$$

where V_{ij} is the potential energy function between atoms i and j, f_A denotes the attractive interaction function between atomic pairs, which is related to the covalent bonding bond energy, f_R is the repulsive interaction function between atomic pairs, which is related to the electron fluctuation orthogonality, the Tersoff potential function takes into account the influence factor of the surrounding environment and introduces the truncation function f_C for interatomic interactions to limit the range of action of the potential function V_{ij}, and r_{ij} denotes the distance between atom i and atom j. The low-valence function b_{ij} contains the interdependence on the bond angle and the many-body interaction, A and B denote the attraction term binding energy and the repulsion term binding energy, respectively, R is the truncation length, β is the bond level coefficient, ζ_{ij} is the bond angle energy, and θ denotes the bond angle between atoms.

2.3. Simulation Environment Settings. In molecular dynamics simulation, the whole system needs to be relaxed after modeling. In order to keep the system temperature in a constant temperature range, transfer the heat induced by the indenter, and ensure the equilibrium state of the system before the friction, the atoms of the constant temperature layer were set at about 300 K using the regular system synthesis (NVT).[25] During the friction simulation, the friction speed was set to 50 m/s and along the negative direction of the Y-axis with a time step of 1 fs in order to save computational time while ensuring the accuracy of the experimental results. The simulation was performed in a massively parallel machine (Lammps)[26] developed by Plimpton. The atomic microscopic changes were monitored in real time by a visualization tool (Ovito)[27] monitored in real time, and the simulation environment parameters are shown in Table 2.

3. RESULTS AND DISCUSSION

3.1. Analysis of Friction Force. 6H-SiC, as a brittle ceramic material, will undergo a certain elastic−plastic deformation by the friction of the diamond grinding tool in the process of friction. Newton's equations of motion and the superposition theorem are the theoretical basis of molecular

Table 2. Simulated Environmental Parameters

relevant parameter	parameter values
ensemble	(NVT)
cutting crystal	(0001)
cutting speed	50 m/s
creasing temperature	300 K
cutting step length	1 fs

dynamics. The interatomic trajectories are derived from the equations of the laws of motion in classical physics. The molecular dynamics method ignores the quantum effect between particles. For particle i, the equation of motion is as follows

$$F_i(t) = m_i a_i(t) \tag{9}$$

The frictional forces Fx, Fy, and Fz in the three directions of the friction process are shown in Figure 2. It can be seen from
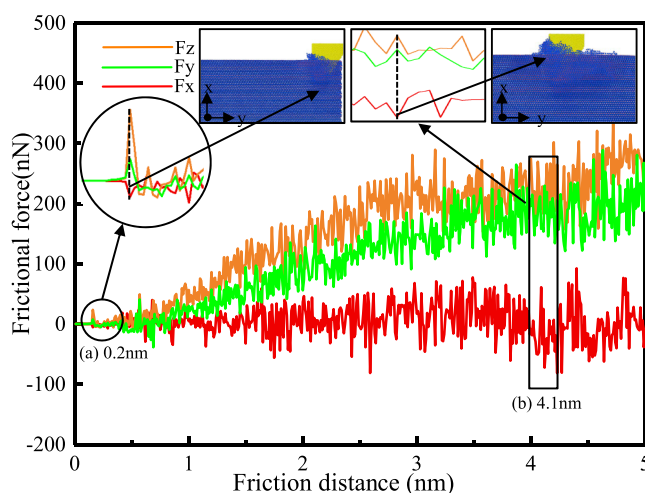
Figure 2. Variation curves of friction in each direction of 6H-SiC.

the figure that with the increase of the friction distance, the frictional forces in different directions change differently, but the general trend is basically the same, with an upward trend. This is due to the fact that in the process of friction, the 6H-SiC workpiece is deformed and phase-transformed in the contact part under the action of shear stress, and the energy transformation in the system, which is accompanied by the breaking of covalent bonds, requires greater frictional force, so the friction force becomes larger; at the same time, some chemical energy is transformed into heat energy and the temperature rises. As can be seen in the figure, the friction force in all directions is 0 at the beginning, and with the increase of distance, the trend of friction force along the Y- and Z-directions is basically the same; moreover, the fluctuation degree does not change much, basically showing a more stable trend and indicating that the simulated friction indentation system is well balanced during the chilling phase. Figure 2 is a graph of the change of friction force in each direction of 6H-SiC, from which it can be seen that with the increase of friction distance, the friction force changes differently in different directions, but the general trend is basically the same: all have an upward trend. This is due to the deformation and phase change in the contact part of the 6H-SiC workpiece under the action of shear stress during the process of friction and the energy transformation in the system. As the process of friction
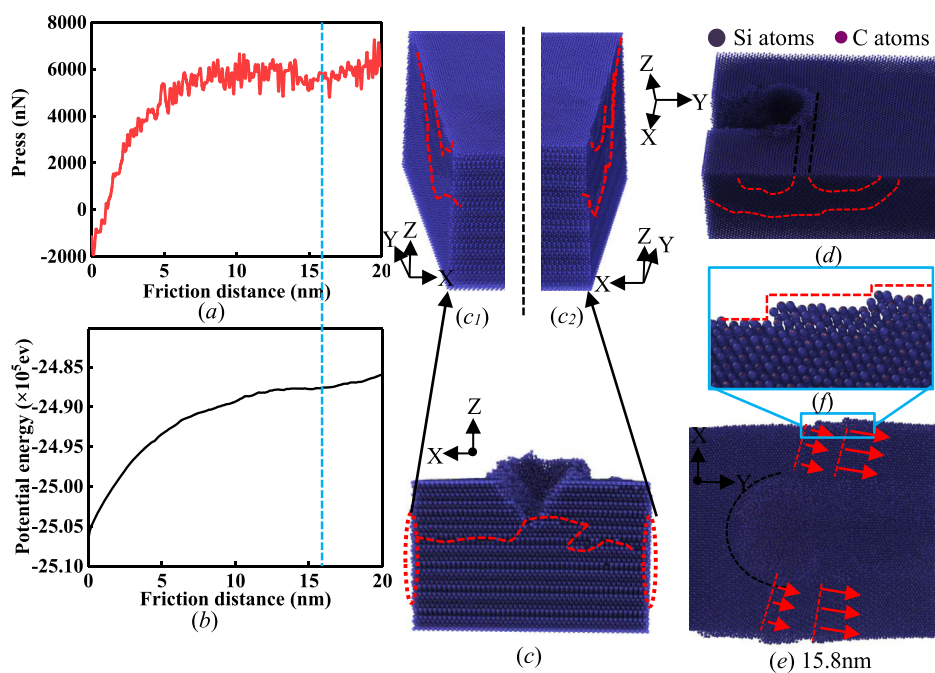
Figure 3. Energy variation curve of the 6H-SiC friction process. (a) Pressure trend diagram. (b) Potential energy trend diagram. (c) Structure diagram of subsurface damage. (c_1) Crystalline surface damage $\langle 1\bar{1}00 \rangle$. ($c_2$) Crystalline surface damage $\langle 1\bar{2}11 \rangle$. (d) Damage main view. (e) Deformation diagram of crystal plane structure [0001]. (f) Partial view of (e).

is accompanied by the breaking of covalent bonds, a greater frictional force is required, while some of the chemical energy is converted into heat and the temperature rises. As can be seen in the figure, the friction force in all directions is 0 at the beginning, and with the increase of distance, the trend of friction force along the Y- and Z-directions is basically the same; moreover, the fluctuation degree does not change much, basically showing a more stable trend and indicating that the simulated friction indentation system is well balanced during the chilling phase. However, there is a certain difference between the friction force along the X-direction and the above two forces. As shown in (a), when the friction distance is 0.2 nm, the friction force decreases for the first time instead of rising in the x-direction, which may be related to the lattice arrangement of 6H-SiC. The X-direction corresponds to the $[10\bar{1}0]$ crystal direction, and the lattice arrangement of 6H-SiC in this direction is a "Z-type" arrangement. The Si–C double-layer arrangement of 6H-SiC is ABCACB–ABCACB, with the perpendicular arrangement of atoms of 6H-SiC in the z-direction, resulting in a blocked friction; the normal force will be larger. The same phenomenon occurs in (b), but the reason for the drop in the X-direction here is that the resistance becomes smaller at 4.1 nm because the tool has formed defects or cracks in the X-direction with larger voids before 4.1 nm.

3.2. Friction Process Energy Change Analysis. In order to have a deeper understanding of the changes during the deformation damage of 6H-SiC, the trend graphs of the friction force as well as the potential energy are extracted in this study, as shown in Figure 3. In Figure 3a, the curve of force basically shows a smooth trend after a continuous rise and no further change, indicating that the system eventually stays in an equilibrium position as time increases during the friction process due to the initial conditions set. The friction force is small at the beginning, and the covalent bonds between the silicon carbide atoms are difficult to break and the required force slowly becomes larger, so the curve keeps showing an

upward trend and basically stops changing at about 7 nm. However, at the friction distance of 15.8 nm, the force decreases, and the potential also shows small fluctuations at this time, as shown in Figure 3b. During the friction, shear stress appears between the contact surface of the tool and 6H-SiC, which is the key to dislocation formation. Due to the increase of shear stress, a delamination phenomenon appears on the workpiece side of 6H-SiC, as shown in Figure 3c. This is due to the fact that in the process of friction, as the workpiece is squeezed by the tool, the top atomic layer transfers the pressure to the bottom, and the system energy rises in the micro-regular system synthesis in order to reach an equilibrium state of energy, leading to intense atomic motion and appearance of the atomic delamination phenomenon. In addition to this, it is found that there is a tendency for the energy to decrease at 15.8 nm, and the corresponding potential energy also decreases and then tends to equilibrium. This is caused by a combination of phase changes in the silicon carbide atoms after lattice reconstruction and the elastic recovery of the machined surface of the silicon carbide workpiece. In order to show the effect of delamination more intuitively, this paper extracts the effect of delamination on both sides of the workpiece, as shown in Figure 3c_1,c_2. (c_1) shows the delamination view on the left side of Figure 3c, which forms two "V" effects during the friction process, and the right side Figure 3c_2 shows the delamination view on the right side of Figure 3c, which presents two "W" delamination effects. This phenomenon is due to the fact that the shear force on the atomic layer differs between the two sides due to the different squeezing forces, which results in different layering effects on the two sides. The diagram in Figure 3d shows that the delamination starts to form at the position below the tool; the atoms on both sides of the frictional groove appear to be crowded out to the sides, and the crowded-out atomic layers are distributed in a step-like pattern at the outer edges, as
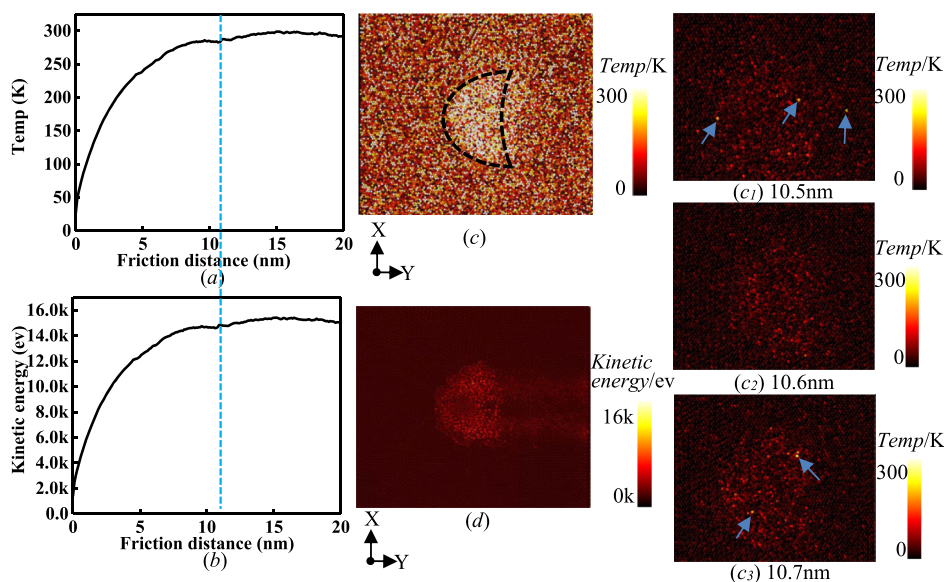
Figure 4. Temperature and kinetic energy curves of the 6H-SiC friction process. (a) Temperature change trend diagram. (b) Kinetic energy change trend diagram. (c) Temperature distribution cloud diagram. (d) Kinetic energy distribution cloud diagram near the tool. (c_1–c_3) Temperature distribution cloud at 10.5, 10.6, and 10.7 nm.
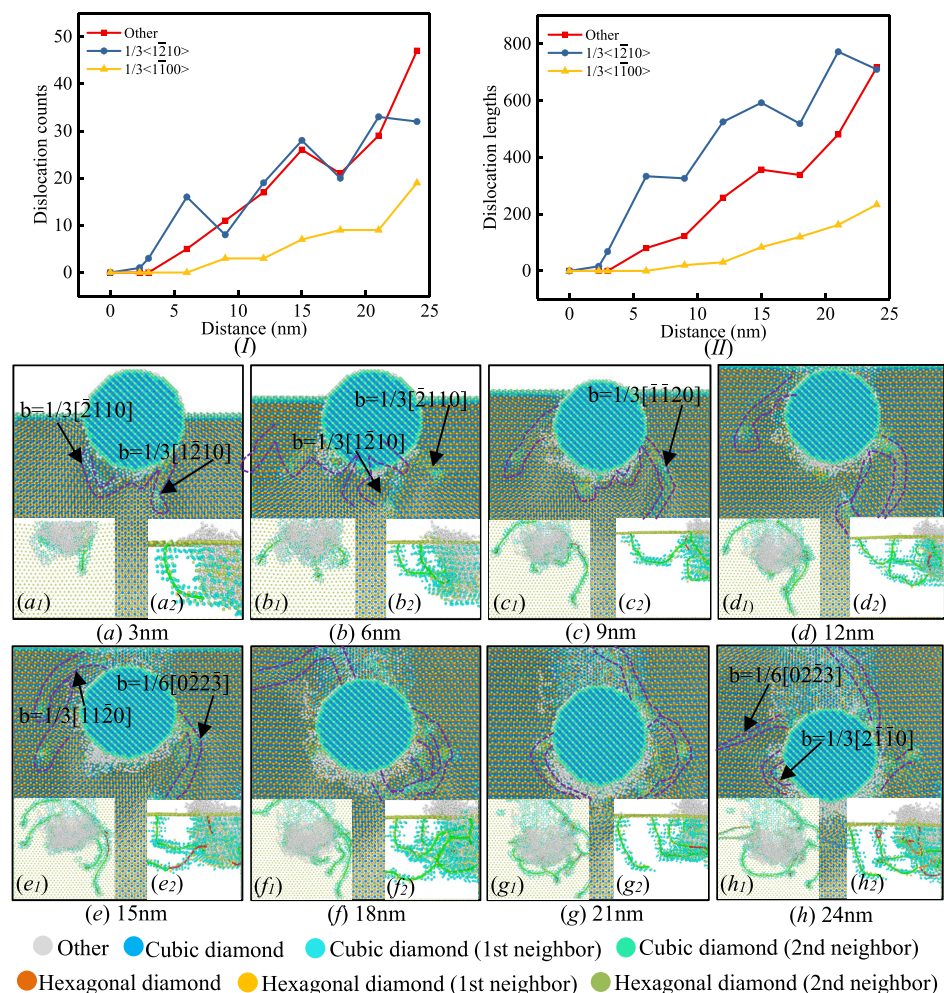

Figure 5. Number and length of dislocations in the friction process and the dislocation evolution diagram: (I) number of dislocations in 6H-SiC. (II) Length of dislocation in 6H-SiC. (a–h) Dislocation extension at 3, 6, 9, 12, 15, 18, 21, and 24 nm. (a_1–h_1) Top view of dislocation extension. (a_2–h_2) Local enlargement of dislocation.

shown in diagram (f). The above phenomenon proves the reason for the formation of the delamination phenomenon.

During the machining process, the changes in friction temperature and kinetic energy affect the wear of the tool and the accuracy of the workpiece, so friction temperature and kinetic energy are important physical quantities for investigating the friction process. The friction temperature generally refers to the average temperature of the polishing area between the diamond tool and the workpiece of 6H-SiC. It can be seen from Figure 4a,b that the temperature and kinetic energy of the workpiece change in almost the same trend. As the friction progress increases, the depth of the tool rubbing the workpiece also increases, and finally, the curve of temperature and kinetic energy basically tends to balance. This is mainly due to the fact that the early friction is the tool applied force and tool and workpiece extrusion; the temperature between atoms gradually increased, accompanied by kinetic energy increase, and at the same time, 6H-sic extrusion shear deformation increased, resulting in 6H-sic workpiece lattice deformation and atomic bond fracture, accompanied by an increase in the amorphous phase. The energy released goes up, the temperature goes up, and the kinetic energy goes up. Since then, the temperature between atoms almost never changes, which is not only related to the system setting. We speculate that some deformation layers may have completely slipped and formed dislocation. The diffusion of dislocation and the movement of atoms require energy consumption, so the energy and temperature of the system almost do not fluctuate and tend to balance. In the equilibrium stage, it is observed that there is a downward trend at the friction distance of 10.6 nm. In order to explore the reason, the temperature distribution cloud map of 6H-SiC at 10.6 nm was obtained by Ovito, as shown in Figure 4c, and the atomic temperature distribution in the figure that is not worn tends to be more uniform. The atomic temperature is higher in the crescent region near the tool, and the cloud map of atomic kinetic energy in Figure 4d also confirms that the atomic kinetic energy around the tool is larger. In order to continue to compare the temperature changes at 10.6 nm, the color of the temperature region is deepened by rendering, and the temperature cloud map changes at 10.5, 10.6, and 10.7 nm are compared, as shown in Figure $4c_1-c_3$. By comparison, it is found that atoms with a higher temperature appear at 10.5 and 10.7 but not at 10.6 nm, which may be due to the breakage of atomic bonds at both 10.5 and 10.7 nm and the bonding between atoms; the force decreases, the number of atoms removed increases, and the temperature increases. In addition, in the friction process, there is not only the formation of amorphousness but also the generation of phase transition; the original atomic bonds are broken, some atoms are recombined to form new covalent bonds, and the temperature will also fluctuate slightly. The crystal structures of internal energy released and consumed largely offset each other but almost will not have too big change, basic into balance.

3.3. Dislocation Analysis.
In the process of friction, the action of the friction blade on the workpiece has three stages, which are the elastic deformation stage, the elastic−plastic transformation stage, and the plastic stage. The plastic stage occurs at the initial stage of friction. In this stage, the friction depth of the tool is shallow, only the surface of 6H-SiC is damaged, the workpiece produces recoverable elastic deformation, and no chips are produced. Figure 5I,II represents the number and length of dislocations in 6H-SiC, respectively, where the dislocation length represents the total dislocation length. In the initial stage, the number and length of dislocations are 0, indicating that no dislocations are generated at this time, and the friction is in the elastic stage. As the friction force gradually increases, when the stress exceeds the yield strength, the workpiece undergoes an elastoplastic transition stage. At this stage, the workpiece material bulges on both sides and in front of the tool, and a deformation layer appears inside; the appearance of the deformation layer is a dislocation of the premise of formation. The time of the above two stages is short and the change is not obvious, and the two stages have little effect on the processing process. The cracks, defects, and damages generated by the friction process of 6H-SiC are the focus of the processing process. Therefore, the plastic deformation stage is the main part in the 6H-SiC friction process, and the sign to judge the plastic deformation is the formation and expansion of dislocations. The dislocation extraction method (DXA) can automatically identify the dislocation changes in the simulation process and indirectly represent the atomic change trajectory through the Burgess vector, which makes the dislocation expansion and fracture slip analysis more intuitive and concrete. In order to observe the changes of dislocations intuitively and accurately, in Figure 5, eight dislocations with different friction distances (3, 6, 9, 12, 15, 18, 21, and 24 nm) were intercepted by the dislocation extraction method (DXA). Expanding the figure, it can be seen from Figure 5I,II that the number and length of dislocations basically show an increasing trend with the increase of friction depth, but the number and length will decrease at certain moments. There are two dislocations formed in (a); the Burgers vector (hereinafter referred to as the Burgers vector) is $b = 1/3[\bar{2}110]$ and $b = 1/3[1\bar{2}10]$ in the figure. In Figure 5b, a new dislocation vector is formed as $b = 1/3[\bar{2}110]$. In Figure 5a,b, it is clearly seen that the dislocations increase at 3 and 6 nm. It is observed in the figure that the dislocation is formed in the area below the cutter head, and the dislocation is continuously expanded outward through the partially enlarged dislocation line diagram (a_2). With the formation of amorphousness, the workpiece has undergone a phase transition, which has lost the original hexagonal structure and transformed into an amorphous state. However, in Figure 5b, the number and length of dislocations are reduced. In Figure 5c, it is observed that due to the increase of frictional stress, the degree of deformation becomes larger, more atomic bonds are broken, atoms move with the stress, some atoms recombine, and two dislocations recombine into one, which also verifies a phenomenon in which the number and length of dislocations are reduced. This feature can also be observed in Figure 5d−h. The dislocations expand from the periphery of the tool in a "claw" shape, and some dislocations form dislocation loops as shown in Figure 5h; the original dislocation breaks when the friction depth is 21 nm (as shown by the vector $b = 1/3[\bar{1}\bar{1}20]$ in Figure 5c). In addition, as shown in the red dislocation line in Figure 5e, there are some incomplete dislocations and other dislocations. It can be observed from Figure 5I,II that the number and length of dislocations of $b = 1/3[1\bar{2}10]$ are significantly larger than those of $b = 1/3[1\bar{1}0]$. This is because the complete dislocation (such as $b = 1/3[1\bar{2}10]$) mostly appears below the tool friction grain, appearing earlier and for a longer time throughout the whole process of the plastic deformation stage. However, incomplete dislocations (such as $b = 1/3[1\bar{1}00]$) are mainly formed at the friction distance of 12 nm, with a shorter length, a shorter duration, and easier fracture, which may be related to
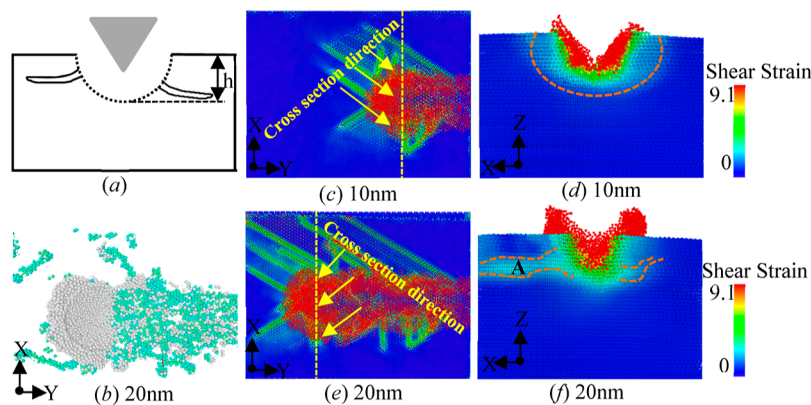
Figure 6. Stress−strain cloud diagram of the 6H-SiC friction process. (a) Mechanical model diagram of indentation fracture. (b) Distribution diagram of friction atoms. (c) Shear strain distribution at 10 nm. (d) Strain distribution in the section view of figure (c). (e) Shear strain distribution at 20 nm. (f) Strain distribution in the section view of figure (e).

the shear stress nearby. After the atom is sheared, another atom replaces the original atom, and the atom moves in a direction, resulting in the change of the lattice structure and the extension of the dislocation.

3.4. Shear Strain Analysis. The generation of dislocation is affected by stress. In order to further understand the influence mechanism of stress and strain on the friction process of 6H-SiC, the shear strain cloud map was extracted. The shear strain cloud map can accurately analyze the stress of the workpiece and the microscopic crack propagation. The shear stress algorithm was used to observe the internal stress and strain under a certain truncation radius. The change of stress is an intuitive reflection of the change of material structure. By calculating the distribution and change trend of shear stress, the change of defects such as phase transformation and dislocation near the grain boundary and the tool under the action of friction can be judged. Meanwhile, the change trend of stress can be predicted with the increase of friction distance. There are crack propagation and the structural failure trend of the 6H-SiC subsurface. Shear stress is expressed by three-dimensional stress tensor

$$\delta_H = \frac{(\delta_x + \delta_y + \delta_z)}{3} \tag{10}$$

$$\delta_V = \sqrt{\frac{(\delta_x - \delta_y)^2 + (\delta_y - \delta_z)^2 + (\delta_z - \delta_x)^2}{2} + 3(\tau_{xy} + \tau_{yz} + \tau_{zx})^2} \tag{11}$$

where δ_x, δ_y, and δ_z and τ_{xy}, τ_{yz}, and τ_{zx} represent each component of the stress tensor. The processing of 6H-SiC ceramics in the brittle zone produces a large number of microscopic cracks, which are related to the joint action of stress, strain, and dislocation. In the theory of fracture mechanics, the scoring effect of the friction tip on the workpiece surface is regarded as a sharp indenter applying a load perpendicular to the material surface, and the crack extension is judged by probing the stress−strain intensity factor of its surface. The crack system caused by the tapered tool is mainly transverse crack. As shown in Figure 6a, in order to explore the induced deformation and cracks, the tool applies a certain rate of increasing normal load to the workpiece surface, and this rate is controlled by the wear depth. The tensile stress generated on both sides and at the bottom of the plastic deformation zone exceeds the strength limit of the material, resulting in transverse microcracks parallel to the

surface of the workpiece. The tensile stresses on both sides and at the bottom of the plastic deformation region exceed the strength limit of the material, resulting in the corresponding dislocations, which lead to transverse microcracks parallel to the workpiece surface. Figure 6 shows the shear stress cloud diagram during the friction process of 6U-SiC, Figure 6c is the section stress cloud diagram at the friction of 10 nm, and Figure 6d is the sectional view. The tool friction depth and the strain in the surrounding area are smaller; when the stress away from the tool is smaller, more stressed atoms are concentrated near the tool. Typically, the bottom shear stress without contact with the indenter is less than 5 GPa. With the increase of the friction depth, the atoms with larger stress increase ceaselessly, and it is obvious that the stress on both sides of the tool extends to both sides; dislocations are formed here and gradually extend outward. At the same time, the expansion of dislocations will lead to more atoms generating large shear stress. Dislocation usually occurs on the slip plane of the crystal plane. Under the action of stress, some atoms move away from their original positions, driving the migration of other atoms and causing the slip of the crystal plane. In the process of slip, dislocation is gradually formed and diffused with the influence of stress and gradually extends outwardly. The extension of dislocation leads more atoms to produce larger shear stress, which ranges from 6 to 8 GPa. Shear stress near the indenter tends to be large, often exceeding 8.5 GPa, as shown in red in Figure d,f. Figure (d) should become more symmetric distribution, mainly concentrated in the tool below. This is because the stress does not spread around and stress did not reach the area; graph (f) shows that stress as dislocation extension of atomic motion has spread involving the A neighborhood and strain with migration, and because both sides have an uneven distribution of stress and strain area, there is A difference too. In the subsequent friction, due to the joint action of stress, strain, and dislocation, it is observed that area A gradually deforms macroscopically, and the workpiece appears with crack or fracture layers. In addition, it is observed that when the depth of the friction tool reaches a certain depth, the formation time and speed of dislocation are different. In the following exploration, we will also focus on exploring the different depths of the tool pressed into the workpiece, which affects the internal microcracks.

3.5. Radial Distribution Analysis. In order to explore the influence of tool depth on the microstructure of 6H-SiC nanofriction, four radial distribution functions at different
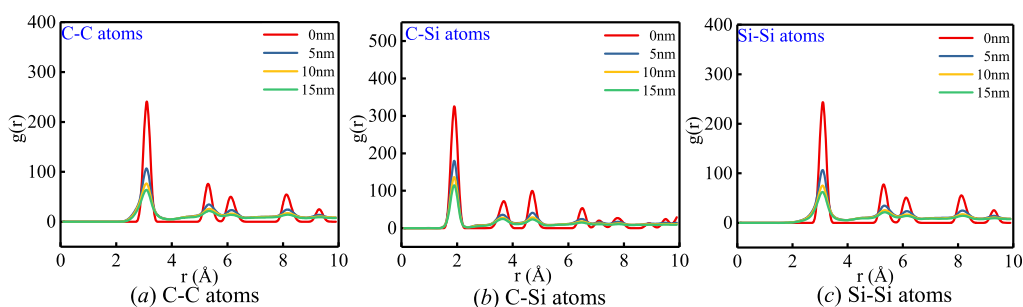
Figure 7. Radial distribution of frictional deformation area at different depths. Radial function distribution at 0, 5, 10, and 15 nm. (a) C−C atoms. (b) C−Si atoms. (c) Si−Si atoms.
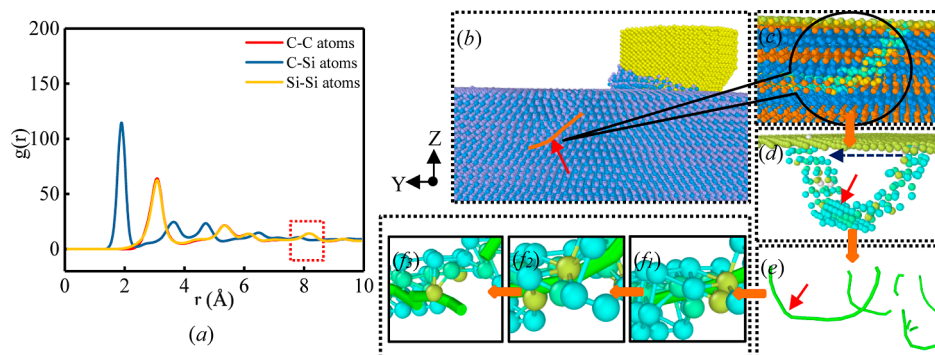
Figure 8. Radial distribution function and dislocation evolution at 15 nm. (a) Radial distribution function diagram at a friction depth of 15 nm. (b−e) Dislocation evolution diagram. (f_1−f_3) Model diagram of dislocation expansion and the fracture ball bond.

depths were selected as examples, as shown in Figure 7, and C−C, C−Si, and Si−Si bond pairs were selected for comparison. The radial distribution function is used to judge the diffusion of atoms in the crystal. When changes occur in the crystal, a large number of amorphous states will be generated. The radial distribution function can more intuitively describe the change of the density of amorphous states. Its expression is

$$g(r) = \frac{n(r)}{\mu_0 V} \approx \frac{n(r)}{4\pi r^2 \mu_0 \lambda r} \qquad (12)$$
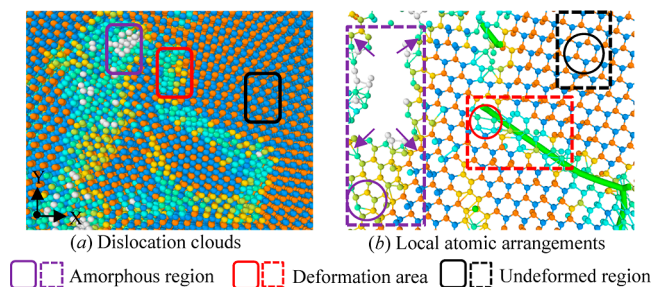
where $n(r)$ is the number of atoms in the spherical shell with thickness λ_r from the target atom r. μ_0 is the number of atoms per unit volume; V is the volume of the spherical shell with radius r and thickness λ_r. The radial distribution function can analyze the distribution of internal atoms and has a certain supporting effect on the analysis of microcrack propagation inside the workpiece. As the depth increases in the figure, the peak of $g(r)$ gradually becomes smaller and the peak value of the main peak decreases, but the position of the maximum value is basically unchanged, indicating that the region where the atomic structure changes during the friction process is basically fixed, the friction depth increases, the interatomic stress increases, the atomic spacing becomes smaller, and the structure becomes smaller. In Figure 7a,c, the peak at the truncation radius r > 8 Å flattens out and disappears when the friction depth is 15 nm, but the C−Si bond pair in Figure 7b has flattened out and has no peak at r > 6 Å. This is due to the fact that the bond energy between C and Si is much smaller than the bond energy between the same atoms. Moreover, the main peak of the C−Si bond pair in Figure 7b is generally much higher than that of C−C and Si−Si bond pairs, indicating that under the same friction depth, the distance

between C and Si in the deformation region is larger, and the atomic bond is easier to break. With the increase of friction depth, dislocations are more likely to nucleate and expand, forming microcracks.

After exploring the radial distribution function, in order to further observe the microscopic changes at 15 nm, as shown in Figure 8, the local atomic arrangement and dislocation map with vector $b = 1/3[\bar{1}2\bar{1}0]$ dislocation at 15 nm were extracted. In the red region of Figure 8a, when the truncation radius r > 8 Å, the curve of the C−Si bond pair no longer has a peak and even has a downward trend, while the C−C and Si−Si bond pairs can clearly see the peak, and a peak appears when the truncation radius r > 9.4 Å. Figure 8b shows the friction nanosimulation at 15 nm; the yellow line part shows that the atoms are irregularly arranged. Figure 8c is a partial magnification of the dislocations, in which it can be seen that the lattice structure has changed and the atoms have migrated a lot to form dislocations, and the dislocations are not generated in the same direction but extend and extend from inside to outside. The shape of the dislocation is not visible in Figure 8c, but the overall shape of the dislocation can be visualized in Figure 8d, where the dislocation is formed below the surface atomic layer and the extension direction is to the left. In order to see the specific situation of the dislocation more intuitively, the system materializes the dislocation and uses the dislocation line to represent the shape of the dislocation, as shown in Figure 8e. When the friction depth increases, the atomic spacing becomes larger due to the influence of stress. When the strength limit of the material is exceeded, the atomic bonds are broken. (f_1−f_3) marks the process of dislocation breaking. Compared with the C−C and Si−Si bond pairs, the distance is much smaller. From the potential function of the system, it can be seen that the

attraction between the same atoms is much larger than the attraction between different atoms, so it is more likely to break. This shows that the peak of the C−Si bond pair is smaller at the radial distribution function of 15 nm, and the truncation radius of the main peak of the C−Si bond pair is higher than that of the other two bond pairs.

3.6. Subsurface Damage Analysis. When the diamond tool rubs the 6H-SiC workpiece, it will go through the elastic deformation stage, the elastic−plastic transformation stage, and the plastic deformation stage in turn, and the first two stages are short in time. In order to study the subsurface damage of the workpiece, the first two stages will not be explored. The plastic deformation stage is mainly discussed. Figure 9 shows

(a) Dislocation clouds   (b) Local atomic arrangements

☐ ⌐ Amorphous region   ☐ ⌐ Deformation area   ☐ ⌐ Undeformed region

Figure 9. Dislocation clouds and local atomic arrangements during the deformation phase.

the dislocation cloud diagram and local atomic arrangement diagram of the deformation stage of the 6H-SiC workpiece, indicating the beginning of the plastic stage, when the dislocations are formed. Three regions are marked in Figure 9a; the purple box represents the amorphous deformed region, the red box represents the deformed region, and the black box represents the undeformed region. The right Figure 9b is an enlarged view of Figure 9a, and the bond angle is added to Figure 9b to facilitate the analysis of the phase transition of the crystal structure during the friction process. The atoms in the undeformed area are arranged in a hexagonal and regular arrangement. With the increase of depth of friction, the friction entered the stage of plastic deformation, and the dislocation tool of the atomic layer near the pressure produces and extends outward; at this time, atomic bonds by stress disconnect, and dislocation lines around the atom are no longer a six-square arrangement and free of some atoms with the pentagon and rectangular shapes; this phenomenon shows that workpiece internal lattice change already occurred at this time. After the atomic bonds are broken, a large number of amorphous crystals are formed due to the increase of atomic spacing. The atoms in the amorphous region are irregularly arranged, and the larger distance causes the crystal structure to change, while the amorphous deformation region spacing gradually expands outward and microcracks are formed, which will accelerate the expansion of microcracks in most dislocation intersection regions and cause damage on the workpiece surface.

4. EXPERIMENTAL VALIDATION

4.1. Experimental Platform. The nanofriction simulation analyzes the friction damage from the microscopic point of view. In order to verify the accuracy of the simulation effect, the experimental part is added to further analyze the damage mechanism from the experimental point of view.

Figure 10 shows the nanofriction experimental platform, which adopts the NHT3 nanoscratch tester. The chemically
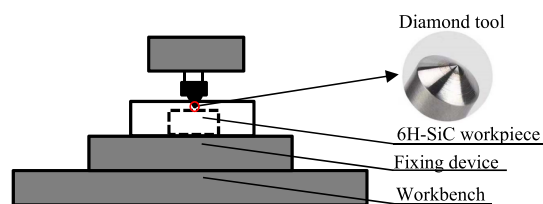
Figure 10. Friction experimental platform model.

and mechanically treated 6H-SiC workpiece is fixed on the working table, and then the table is moved to fix the diamond tool to rub the 6H-SiC workpiece at a speed of 50 m/s with a friction depth of 0.01 mm. The friction surface is the [0001] crystal surface with the direction inward, and the workpiece is kept fixed during the rubbing process. A Hitachi S-4700 scanning electron microscope and a transmission electron microscope, Hitachi H-9000NAR, were tested to observe the internal changes after friction.

4.2. Experimental Validation. Figure 11 shows the surface damage map and a partial enlarged view of 6H-SiC
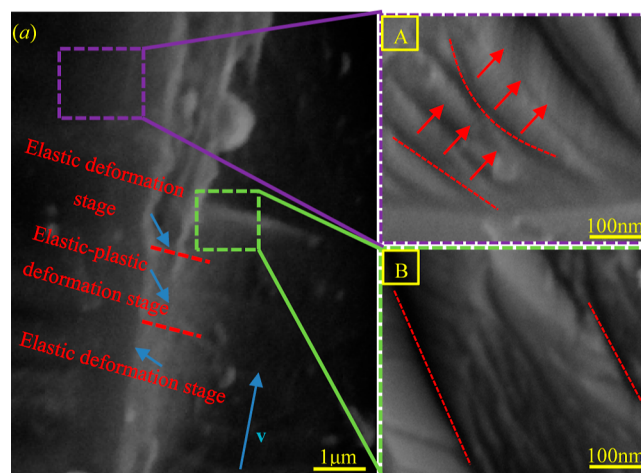

Figure 11. Surface friction damage and local magnified SEM. (a) Image of the friction. A is the purple dotted box area in (a). B is the green dotted box area in (a).

after friction. Figure 11a shows the scratches on the surface after rubbing, and the direction of rubbing is marked with red arrows. As mentioned above, friction is divided into three stages: the elastic deformation stage, elastic−plastic deformation stage, and plastic deformation stage. It can be seen from the figure that the friction is relatively smooth, and the chips do not appear in the two deformation stages of elasticity and elastoplasticity. It can be seen from the figure that the friction is relatively smooth in the two deformation stages of elasticity and elastoplasticity, no chips appear, and the non-friction areas on both sides are relatively smooth. Due to improper chemical and mechanical treatment in the early stage, there are some pits on both sides. However, according to the images in the plastic deformation stage, the crystal has changed and some amorphous features can be found in the surrounding area. In area A, bulges on both sides have been clearly seen, and uneven cracks appear, which is consistent with the simulation effect in Figure 3e. At the same time, a fracture phenomenon

was also found at B. After enlarging the B area, it was seen that due to the stress of the friction cutter head, the side surface of the 6H-SiC workpiece was broken, and there were lumps falling off. The cracks near the upper surface were relatively large, and the cracks continue to expand downward, and the expansion path is irregular. When the gap between the two gaps is large, a gap is formed on the subsurface, and the workpiece peels off and falls off with the gap. It can be seen that the expansion of such cracks is the main form of fracture of 6H-SiC workpieces.

We continue to enlarge the block-shaped peeling area. The crack depth in this part is shallow, and the arrangement is relatively regular. It is initially judged that the crack is just formed. The wrinkle-like area appeared in the lower area of the tool, which was preliminarily determined to be dislocation. Compared with the enlarged picture, it was found that there were more filament-like strips similar to dislocation in the wrinkle-like area. Thus, the former wrinkle-like area was found to be the crystal plane slip state, as shown in (a) of Figure 12.
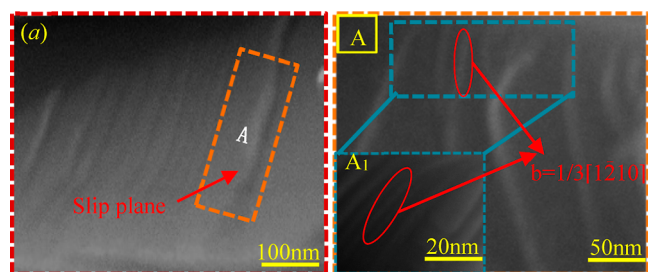
Figure 12. SEM images of the plastic deformation area and TEM images of dislocation (a). SEM local image of the plastic deformation area. A is the dotted wireframe diagram in (a). A_1 is the TEM image of area A.

However, the strips found in the latter magnification are dislocations, as shown in the enlarged view of area A in Figure 12, in which multiple dislocations are concentrated on the slip plane. After zooming in, it can be seen that the multiple cracks are not closely arranged, and the lengths are different. The strip-shaped cracks below the tool are shorter, and the strip-shaped cracks in the area that have been rubbed are longer. Therefore, the crack was determined to be formed by transverse dislocation propagation. One of the dislocations was selected in the experiment, and the vector of the dislocations was found to be $B = 1/3[1\bar{2}10]$, as shown in the ellipse marked in red. The arrangement of dislocations can be clearly seen from the TEM image. The dislocations on both sides are longer, but the dislocations below the tool are shorter, and this area is more prone to fracture and recombination of dislocations, which is similar to Figure 6 above. The simulated phenomena are basically consistent, indicating that dislocations are the basis for the formation of subsurface damage.

5. CONCLUSIONS

1. The friction forces in the three directions are obviously different during the subsurface damage process of 6H-SiC nanofriction using molecular dynamics simulation, and the friction force in the X-direction is significantly smaller than that in the Y- and Z-directions. The kinetic energy, potential energy, temperature, and acting force in the friction process basically showed an upward trend, and the flank of the 6H-SiC workpiece was accompanied by the formation of falling blocks and cracks. Due to the stress generated by friction, dislocations appear near the friction of the diamond tip, and most of them appear as lateral dislocations. The dislocation formation and expansion process is accompanied by energy exchange. Cracks and exfoliated blocks constitute the subsurface damage of the 6H-SiC workpiece on a macroscopic scale.

2. The microscopic crystal changes and the formation of macroscopic cracks were compared by friction experiments, which supplemented the analysis of the subsurface damage mechanism experiments of simulating nanofriction 6H-SiC. The analysis and exploration of the subsurface damage mechanism of simulated 6H-SiC nanofriction provide a certain guiding significance for the realization of high-precision machining of 6H-SiC precision devices.

■ AUTHOR INFORMATION

Corresponding Author

Nanxing Wu − *School of Mechanical and Electronic Engineering, Jingdezhen Ceramic Institute, Jingdezhen 333403 Jiangxi, China; Laboratory of Ceramic Material Processing Technology Engineering, Jingdezhen 333403 Jiangxi, China;* ⊙ orcid.org/0000-0001-8544-4417; Email: jxlocmpte_vip@163.com

Authors

Dongling Yu − *School of Mechanical and Electronic Engineering, Jingdezhen Ceramic Institute, Jingdezhen 333403 Jiangxi, China*

Huiling Zhang − *School of Mechanical and Electronic Engineering, Jingdezhen Ceramic Institute, Jingdezhen 333403 Jiangxi, China*

Xiaoyu Feng − *School of Mechanical and Electronic Engineering, Jingdezhen Ceramic Institute, Jingdezhen 333403 Jiangxi, China*

Dahai Liao − *School of Mechanical and Electronic Engineering, Jingdezhen Ceramic Institute, Jingdezhen 333403 Jiangxi, China*

Complete contact information is available at:
https://pubs.acs.org/10.1021/acsomega.2c02115

Author Contributions

§D.Y. and H.Z. contributed to the work equally and should be regarded as co-first authors.

Notes

The authors declare no competing financial interest.

■ REFERENCES

(1) Zhang, Y. X.; Guo, S. C.; Ku, W.; Wang, D.; Wang, J. Mechanical Behavior and Simulation analysis of Single crystal SiC Micro-nano Indentation. *Piezoelectrics Acoustooptics* **2018**, *40*, 742−745.

(2) Zhang, G. H.; Wang, G. L.; Wang, Z. G.; Xu, Y. J. Effect of Pressure on nano-polished Silicon carbide based on Molecular Dynamics. *Heavy Machinery* **2018**, *346*, 25−29.

(3) Gao, Y.; Yan, W.; Gao, T.; Chen, Q.; Yang, W.; Xie, Q.; Tian, Z.; Liang, Y.; Luo, J.; Li, L. Properties of the structural defects during SiC-crystal-induced crystallization on the solid-liquid interface. *Mater. Sci. Semicond. Process.* **2020**, *116*, 105155.

(4) Goel, S.; Luo, X.; Comley, P.; Reuben, R. L.; Cox, A. Brittle-ductile transition during diamond turning of single crystal silicon carbide. *Int. J. Mach. Tool Manufact.* **2013**, *65*, 15−21.

(5) Li, Z.; Zhang, F.; Luo, X. Subsurface damages beneath fracture pits of reaction-bonded silicon carbide after ultra-precision grinding. *Appl. Surf. Sci.* **2018**, *448*, 341−350.

(6) Goel, S.; Yan, J.; Luo, X.; Agrawal, A. Incipient plasticity in 4H-SiC during quasistatic nanoindentation. *J. Mech. Behav. Biomed. Mater.* **2014**, *34*, 330−337.

(7) Yin, Z.; Zhu, P.; Li, B. Study of Nanoscale Wear of SiC/Al Nanocomposites Using Molecular Dynamics Simulations. *Tribol. Lett.* **2021**, *69*, 38.

(8) Zhou, P.; Li, J.; Wang, Z.; Chen, J.; Li, X.; Zhu, Y. Molecular dynamics study of the removal mechanism of SiC in a fixed abrasive polishing in water lubrication. *Ceram. Int.* **2020**, *46*, 24961−24974.

(9) Meng, B.; Yuan, D.; Xu, S. Study on strain rate and heat effect on the removal mechanism of SiC during nano-scratching process by molecular dynamics simulation. *Int. J. Mech. Sci.* **2019**, *151*, 724−732.

(10) Lu, J.; Luo, Q.; Xu, X.; Huang, H.; Jiang, F. Removal mechanism of 4H- and 6H-SiC substrates (0001 and 0001) in mechanical planarization machining. *Proc. Inst. Mech. Eng., Part B* **2019**, *233*, 69−76.

(11) Wang, J.; Fang, F.; Zhang, X. Nanometric Cutting of Silicon with an Amorphous-Crystalline Layered Structure: A Molecular Dynamics Study. *Nanoscale Res. Lett.* **2017**, *12*, 41.

(12) Fang, F.; Xu, F.; Lai, M. Size effect in material removal by cutting at nano scale. *Int. J. Adv. Des. Manuf. Technol.* **2015**, *80*, 591−598.

(13) Wu, Z.; Liu, W.; Zhang, L. Revealing the deformation mechanisms of 6H-silicon carbide under nano-cutting. *Comput. Mater. Sci.* **2017**, *137*, 282−288.

(14) Noreyan, A.; Amar, J. G.; Marinescu, I. Molecular dynamics simulations of nanoindentation of -SiC with diamond indenter. *Mater. Sci. Eng., B* **2005**, *117*, 235−240.

(15) Zhou, P.; Zhu, N.; Xu, C.; Niu, F.; Li, J.; Zhu, Y. Mechanical removal of SiC by multi-abrasive particles in fixed abrasive polishing using molecular dynamics simulation - ScienceDirect. *Comput. Mater. Sci.* **2021**, *191*, 110311.

(16) Duan, N.; Huang, S. G.; Yu, Y. Q.; Huang, H.; Xipeng, X. U. The Material Removal Mechanism of Monocrystal SiC Scratching by Single Diamond Grit with Different Tip Radius. *J. Mech. Eng. Sci.* **2017**, *53*, 171−180.

(17) Ruestes, C. J.; Bringa, E. M.; Gao, Y.; Urbassek, H. M. Molecular Dynamics Modeling of Nanoindentation. *Appl. Nanoindentation Adv. Mater.* **2017**, *14*, 313−345.

(18) Tian, Z.; Xu, X.; Jiang, F.; Lu, J.; Luo, Q.; Lin, J. Study on nanomechanical properties of 4H-SiC and 6H-SiC by molecular dynamics simulations. *Ceram. Int.* **2019**, *45*, 21998−22006.

(19) Xiao, G.; To, S.; Zhang, G. The mechanism of ductile deformation in ductile regime machining of 6H SiC. *Comput. Mater. Sci.* **2015**, *98*, 178−188.

(20) Greiner, C.; Liu, Z.; Strassberger, L.; Gumbsch, P.; Peter, G. Sequence of Stages in the Microstructure Evolution in Copper under Mild Reciprocating Tribological Loading. *ACS Appl. Mater. Interfaces* **2016**, *8*, 15809−15819.

(21) Zhang, L.-C.; Tanaka, H. On the Mechanics and Physics in the Nano-Indentation of Silicon Monocrystals. *JSME Int. J.* **1999**, *42*, 546−559.

(22) Zhang, L.; Tanaka, H. Atomic scale deformation in silicon monocrystals induced by two-body and three-body contact sliding. *Tribol. Int.* **1998**, *31*, 425−433.

(23) Balint, D. S.; Deshpande, V. S.; Needleman, A.; Van der Giessen, E. Discrete dislocation plasticity analysis of the wedge indentation of films. *J. Mech. Phys. Solid.* **2006**, *54*, 2281−2303.

(24) Tersoff, J. Modeling solid-state chemistry: Interatomic potentials formulticomponent systems. *Phys. Rev. B: Condens. Matter Mater. Phys.* **1990**, *39*, 5566−5568.

(25) Zhu, B.; Zhao, D.; Tian, Y.; Wang, S.; Zhao, H.; Zhang, J. Study on the deformation mechanism of spherical diamond indenter and its influence on 3C-SiC sample during nanoindentation process via molecular dynamics simulation. *Mater. Sci. Semicond. Process.* **2019**, *90*, 143−150.

(26) Plimpton, S. Fast Parallel Algorithms for Short-Range Molecular Dynamics. *J. Comput. Phys.* **1995**, *117*, 1−19.

(27) Stukowski, A. Visualization and analysis of atomistic simulation data with OVITO-the Open Visualization Tool. *Model. Simulat. Mater. Sci. Eng.* **2010**, *18*, 015012.